

Prominence eruptions as precursors of coronal mass ejections

Peter Duchlev

Institute of Astronomy and NAO, Bulgarian Academy of Sciences, BG-1784, Sofia,
duchlev@astro.bas.bg

(Submitted on 08.08.2020. Accepted on 09.09.2020)

Abstract. Prominence eruptions (PEs) are one of the fundamental precursors of coronal mass ejections (CMEs). Moreover, PEs play a crucial role in triggering CMEs. Therefore, understanding the initiation and evolution of the erupting prominences provides a crucial physical understanding of the CME initiation and evolution, as well its broader impacts on space weather and geospace climate. This review focuses on the PEs and their associated CMEs in five events. Three events represent an eruption of a single prominence/filament flux rope (FR). The other events present interaction and eruption of two nearby FRs of the same prominence. The five events differ from one another by the type, pre-eruption and eruption evolution of PEs and specific properties of the linked CMEs. The magnetic properties of the source region and overlying magnetic arcade as main factors for the specific physical linkage between PE and CME are discussed for the five events.

Key words: Sun: Prominence/Filament eruptions, Coronal mass ejections, Flares, Active regions, Streamers, Magnetic helicity, EUV radiation, Radio bursts, Multiwavelength observations

1. Introduction

1.1. Prominence basic properties, magnetic environment and associated eruptive events

The solar prominences (or filaments when observed on the disk) are large magnetic structures filled with cool ($T \sim 10^4$ K) and dense ($n_e \sim 10^{11}$ cm $^{-3}$) plasma suspended in hotter ($T \sim 10^6$ K) and tenuous ($n_e \sim 10^8$ cm $^{-3}$) solar corona. Detailed summaries of the prominence properties are given in recent reviews of Labrosse et al. (2010), Mackay et al. (2010), Parenti (2014), and McCauley et al. (2015). The prominences/filaments are formed above the magnetic polarity inversion line (PIL) in a magnetic structure called a filament channel, in which the filament can be supported by the magnetic field (e.g. Martin, 1998 and references therein).

In terms of the magnetic environment of the PILs, there are three essential cases of the prominence formation: (i) in the weak magnetic fields at high latitudes (e.g. polar crown); (ii) within active regions (ARs), and (iii) at the borders of ARs or between two closely situated ARs (Leroy, 1989; Engvold, 1998; Mackay et al., 2010). The prominences are found to form in magnetic dip regions located in two main magnetic configurations: a sheared arcade and a flux rope (FR). In the sheared arcade configuration, the arcade connects opposite polarities on either side of a PIL, whereas in the case of a FR configuration the magnetic field has helical structure (Mackay et al., 2010).

When quiescent prominences/filaments have been observed edge on at the limb, they are often seen to be embedded in relatively dark cavities at the base of coronal helmet streamers (Engvold, 1989). The cavities are the limb counterpart to the filament channel on the disk (Gibson et al., 2006).

Coronal cavities are the multi-thermal regions of hot plasma with temperatures ($\sim 1\text{--}2$ MK) that are slightly higher than those in the surrounding streamer (Fuller et al., 2008; Vasquez et al., 2009; Habbal et al., 2010; Reeves et al., 2012) and plasma density depletion relative to the streamer of 25% in white-light observations (Fuller and Gibson, 2009) and of 30% in extreme-ultraviolet (EUV) observations (Schmit and Gibson, 2011). Moreover, many observational and numerical studies indicate that the magnetic structure of cavities could be well described by a twisted/helical magnetic FR (see Chen et al., 2018, for detailed review).

The prominence-cavity systems show dynamic behavior, even in non-erupting state, which suggest that the prominence and its surrounding cavity is an integrated system in which continuous mass exchange may occur between them (see, e.g. Zhang and Ji 2018, and references therein). The cavities-prominence events are the manifestation of three-part magnetic systems that exist in the low quiet-Sun corona for a long period of time before they erupt bodily as coronal mass ejections (CMEs) (Gibson et al., 2006; Maričić et al., 2009; Forland et al., 2013). Hence, investigations of the magnetic structures of quiescent cavity-prominence systems offer important clues to the nature of magnetic fields in the corona prior to and during CME eruptions (Gibson et al., 2006; Chen et al., 2014).

It is commonly accepted that the prominence/filament eruptions, CMEs and flares are different manifestations of a large single magnetically driven process in the solar atmosphere (e.g. Forbs, 2000; Lin et al., 2003; Su et al., 2011). Many observational studies found a strong but not perfect correlation between the prominence eruptions (PEs) and CMEs because of the various data taken in the different phases of the solar cycle and PE definitions (e.g. Gopalswamy et al., 2003, Bao et al., 2007, Gopalswamy, 2015 and reference therein). The high degree association of the PEs with CMEs suggests a close physical relationship between them that is still not completely understood. Moreover, the observations of PEs that involve CMEs during the past few decades found close spatial and temporal proximity of the two events, which infers that PEs are an integral part of CMEs (see, e.g. Schrijver et al., 2008; Liu et al., 2012; Parenti, 2014; Gopalswamy, 2015; and reference therein). Indeed, as the early studies show, the CMEs originating at the solar limb often exhibit a classic, three-part morphology of a bright leading edge, followed by a dark cavity with a bright core that can be identified as PE (e.g. Illing & Hundhausen, 1986; Dere et al., 1997) Thus, the CME three-part structure is a high coronal equivalent of the prominence-cavity system in the low corona. Therefore, a detailed study of the origin and evolution of PEs is a critical aspect for understanding of their crucial role in triggering CMEs (Schmieder et al., 2013), as well for the CMEs and associated space weather forecasting.

1.2. Prominence eruptions

The PEs show large variety that includes type of eruption, eruption symmetry and direction, apparent twisting and writhing motions, the presence of vertical threads and coronal cavities, CME associations, and kinematics (see, e.g. McCauley et al., 2015). The prominences/filaments can erupt in

many different ways depending on their magnetic environment at all levels of the solar atmosphere and physical processes occurring therein (e.g. Joshi & Srivastava, 2011 for reviews).

The prominences/filaments could undergo three types of eruptions, such as full, partial or failed (Gilbert et al., 2007). In a full eruption, almost all of the filament mass and the magnetic structure escape Sun and produce a CME (e.g. Gilbert et al., 2000; Williams et al., 2005; Shen et al., 2012; Joshi et al., 2014). In a partial eruption, due to magnetic reconnection inside the filament FR, some upper part erupts, expelling some or none of the filament mass that could evolve a CME, while the rest does not erupt (e.g. Gilbert et al., 2000; Gibson & Fan, 2006; Tripathi et al., 2009; Shen et al., 2012; Koleva et al., 2012). During a failed eruption, the filament FR and material remain confined in the corona even after strong disturbances (e.g. Ji et al., 2003; Török & Kliem, 2005; Liu et al., 2009; Kumar et al., 2011; Joshi et al., 2013a; Duchlev et al., 2016; Dechev et al., 2018). A reformation of the filament is another important feature that is often observed after partial and failed filament eruptions (e.g. DeVore & Antiochos, 2008; Tripathi et al., 2009; Koleva et al., 2012; Joshi et al., 2014; Dechev et al., 2018).

There are several mechanisms related to the ambient magnetic field that are able to accumulate coronal magnetic energy and can initiate eruptive instability: (i) magnetic emergence (e.g. Feynman & Martin, 1995; Chen & Shibata 2000), (ii) shearing and/or converging photospheric motions (e.g. Aulanier, 2014), (iii) magnetic cancellation (e.g. Chae et al., 2001; Sterling et al., 2007), and (iv) a change of magnetic connectivity in overlying arcade (e.g. Kong et al., 2013). The mechanisms that have been proposed to trigger solar eruptions can be divided into two groups: (i) ideal MHD instability or loss of equilibrium and (ii) nonideal magnetic reconnection. The first group includes kink instability (Fan & Gibson 2007), torus instability (Kliem & Török 2006; Kliem et al. 2014), or loss of equilibrium (Forbes 1990; Lin & Forbes 2000). The flux emergence model (Chen & Shibata 2000), the flux cancellation model (van Ballegoijen & Martens 1989), and the breakout model (Antiochos et al. 1999) belong to the second category. Detailed reviews about the trigger mechanisms of the solar eruptions can be found in Aulanier (2014) and Green et al. (2018).

1.3. Interactions between nearby prominences and sympathetic prominence eruptions

The interactions between two nearby filaments can cause their eruptions and can lead to a flare and/or a CME (Jiang et al., 2014; Zhu et al., 2015; Yang et al., 2017; Cheng et al. 2018, for reviews). The eruptions due to filaments merging interaction via magnetic reconnection have been reported in some observational studies (e.g. Su et al., 2007; Kumar et al., 2010; Bi et al., 2012; Li & Ding, 2012; Liu et al., 2012; Kong et al., 2013; Yang et al., 2016) and modeled in numerical studies (e.g. Linton et al., 2001; DeVore et al., 2005; Aulanier et al., 2006; Török et al., 2007). Moreover, recent observations showed that branches or FRs of the same filament erupt due to splitting interactions via magnetic reconnection that rapidly change the

magnetic connectivity in the filament (e.g. Kim et al., 2001; Thompson, 2011; Bi et al., 2012; Liu et al., 2012, Dechev et al., 2018; Cheng et al. 2018).

The Sun also produces sympathetic eruptions, which represent a sequence of eruptions occurring within a relatively short time period (tens of minutes to few hours) either in one complex AR (e.g. Liu et al., 2009) or in different, often widely separated regions (Zhukov & Veselovsky, 2007), between which apparent causal relations exist (e.g. Jiang et al., 2009; Liu et al., 2009a; Jiang et al., 2011; Schrijver & Title, 2011; Shen et al., 2012; Yang et al., 2012b; Joshi et al., 2016; Wang et al., 2018).

Studies of sympathetic FEs/PEs have been reported during solar cycle 24, which typically occur as coupled FEs in the quiet-Sun regions (e.g. Schrijver & Title, 2011; Yang et al., 2012b) or as coupled FEs/PEs in ARs (e.g. Schrijver et al., 2011, 2013; Shen et al., 2012). The physical nature of FEs provides opportunity for detailed topological analysis of the source-surface background field of the sympathetic events (Titov et al., 2012), as well as for revealing of the background field main topological elements (see Schrijver & Title, 2011). The results of such analyses are used for numerical modeling and simulations, which reproduce important aspects of the magnetic field overlying sympathetic events. For example, Török et al. (2011) found by simulation that the presence of a pseudo-streamer is important for producing the "twin-filament" eruptions seen in the observations (Török et al., 2011; Titov et al., 2012; Lynch & Edmondson, 2013; Panasenco et al., 2013). Lynch & Edmondson (2013) presented a 2.5D MHD simulation of sympathetic magnetic breakout FEs from a pseudo-streamer source region.

1.4. Homologous prominence eruptions

Among a variety of eruptive behaviors from multiple types, one can distinguish a specific class of homologous eruptions (Zhang & Wang, 2002; Chertok et al., 2004; Kienreich et al., 2011). They exhibit sequences of two or more similar eruptions occurring at the same place only hours to a day or so apart. Recently, Li and Zhang (2013) generalized the homology definition for flares, FEs and CMEs in terms of FR MHD: (i) the homologous FRs originate from the same region within the same AR; (ii) the endpoints of homologous FRs are anchored at the same location; (iii) the morphologies of the homologous FRs must also resemble each other.

The homologous PEs/FEs are still rarely reported events. Zhou et al. (2006) studied two homologous FEs that occurred on 2002 Dec. 28 and were located in an extended bipolar region and beneath multi-arcade system. The first FE was confined and second one presented partial eruption followed by a CME. Similar case was reported by Yan et al. (2012), who studied the eruption of a S-shaped filament on 2000 February 9 to 10. The filament underwent two homologous eruptions, a failed one followed by a full eruption, which was accompanied with a C7.3 flare and led to a halo CME.

Four homologous eruptions of a filament on 2005 July 29 in AR 10792 and beneath a double-arcade system were studied by Jiang et al. (2009).

The FEs were accompanied by flares and associated with CMEs. Four homologous FR eruptions, occurring in AR 11745 on 2013 May 20–22, were reported by Li & Zhang (2013). The first three FRs are associated with failed FEs, while the fourth, fast eruption was identified as a partial filament eruption that was accompanied by a M5.0 flare and a CME. The event on 2006 August 22 represented a sequence of four homologous non-radial PEs, whose source was a filament in AR 10904, located beneath the northern edge of an overlying helmet streamer (Duchlev et al., 2014, 2016). All PEs were of the failed type and the third of them was associated with a narrow CME.

The present review is devoted to five eruptive events of PEs/FEs linked to a CME. It is organized as follows: in Section 2 three events showing a single prominence/filament eruption are reviewed; in Section 3 two events showing interaction and eruption of two nearby FRs of the same filament are reviewed; the final Section 4 contains a summary of global issues related to the five PE/CME events and their discussion.

2. An eruption of a single prominence/filament flux rope

2.1. Prominence eruption on 2010 March 30

The PE occurred at the north-east solar limb between 17:30 UT and 19:30 UT at a mean position angle 66° and represented a height-expanding twisted loop with legs anchored in the chromosphere. Its source filament was located in a quiet-Sun plage region. The PE was observed from the Atmospheric Imaging Assembly (AIA) (Lemen et al., 2012) onboard the Solar Dynamics Observatory (SDO) (Fig. 1) and the Extreme Ultraviolet Imager (EUVI) (Howard et al., 2008) onboard the STEREO B in He II 304 Å channel (Fig. 2).

Just before the activation at 17:19 UT, the prominence was well seen in $H\alpha$ images obtained by the Polarimeter for Inner Coronal Studies (PICS) instrument at the Mauna Loa Solar Observatory (MLSO), Hawaii, as few bright clouds above the limb. A half hour later the prominence body showed the first signature of a twisted FR. The prominence fine structure showed a counter-clockwise twist of one turn (2π) around the FR main axis, as estimated at the time when the beginning of the prominence’s slow rise was observed. The full amount of the prominence twist in the AIA 304 Å images was first seen at around 18:20 UT, and later the total twist of the eruptive prominence FR was estimated to be about 6π (3 turns) (Koleva et al., 2012). This is significantly above the critical value of 2π for kink instability to work (Hood & Priest, 1981).

The different view point of STEREO B and the larger EUVI FOV allow to see the counter-clockwise kink-writhing motion of the filament FR, which was only suggested in the AIA FOV. In contrast with the AIA images, the left-handed kink-writhing motion of the FR loop-like axis was well seen in projection on the disk in the EUVI B images (Fig. 2). The crossing point was visible at approximately half of the filament FR height, which suggests that the FR twist progressively converted into a counterclockwise kink-writhe. Later, when the crossing point descended to one third of the FR

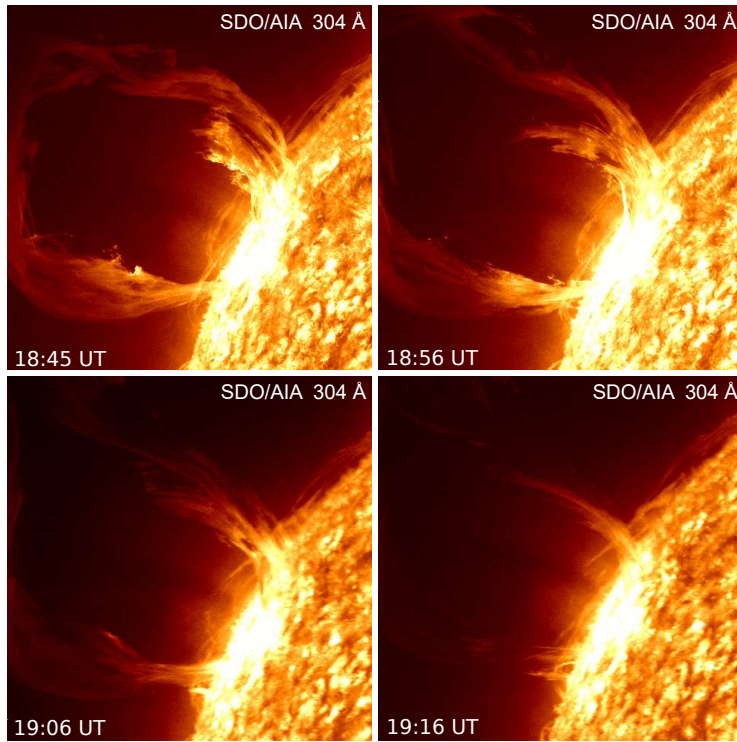


Fig. 1. AIA/SDO He II 304 Å images showing the morphology and, in particular, the helicity evolution of the erupting prominence.

height above the FR feet, the writhing angle increased with time, reaching $\pi/2$, i.e. 1/4 turn (Fig. 2). This result suggests that the PE on 2010 March 30 was possibly kink induced one, although other instabilities should not be excluded.

The PE clearly showed three phases in AIA FOV: an activation, an acceleration, and a constant velocity phase (Koleva et al., 2012). During activation, the prominence slowly rose with a projected velocity of 10 km/s. In the second phase, the prominence rapidly rose up to 121 Mm with increased velocities from 15 km/s to 166 km/s and acceleration between 46 m/s² and 430 m/s². During the third phase, the prominence rose with constant velocity of 91 km/s up to a maximum height reached in the AIA FOV of almost 300 Mm. The real PE maximum height, estimated in the EUVI B FOV, was 526 Mm at 19:16 UT. After that time the prominence descent with velocity of ~ 50 km/s to its primary location where the filament partially reformed two days after the eruption. This suggests a failed type of eruption.

Despite the failed type of the PE, it was associated with a CME with width 64° and position angle 74°. As observed by the Large Angle and Spectrometric Coronagraph (LASCO)/C2 onboard SOHO (Brueckner et

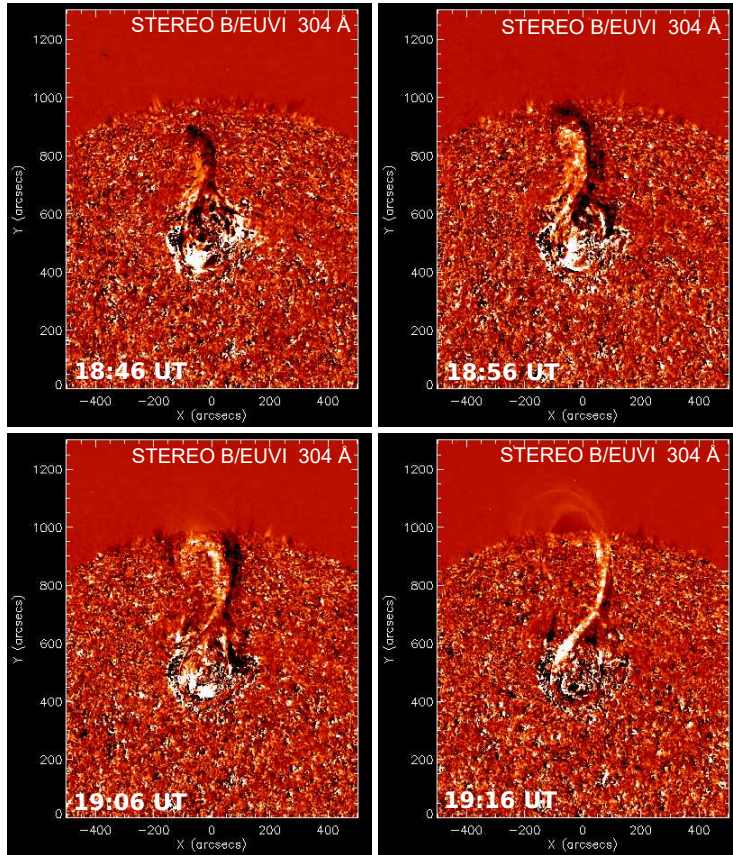


Fig. 2. Running difference images from EUVI/STEREO B in the He II 304 Å channel showing the morphology and the kink evolution of the erupting filament. Frames reproduced from Koleva et al. (2012).

al., 1995), the PE appeared in the northern CME periphery and was associated with a faint narrow loop with a cavity underneath that is part of the large scale CME system (Fig. 3). The CME started at 18:30 UT, a half hour after the PE onset. The CME propagated with an average linear velocity of 724 km/s. Its second-order velocity decreased from 853 km/s to 599 km/s into the LASCO/C2 FOV at a deceleration of -16.4 m/s^2 .

The PE was located underneath a narrow expanding loop with a cavity, which was part of the CME northern periphery (see Fig. 3). Therefore, the PE had a strongly asymmetric position with respect to the overlying magnetic field. The important role of asymmetric overlying field for the failed (confined) type of filament eruptions was pointed out in several observational studies (Ji et al., 2003; Török & Kliem, 2005; Liu et al., 2009b; Guo et al., 2010; Shen et al., 2011; Kumar et al., 2011; Kuridze et al., 2013; Joshi et al., 2014). Apart from these observational studies, numerical sim-

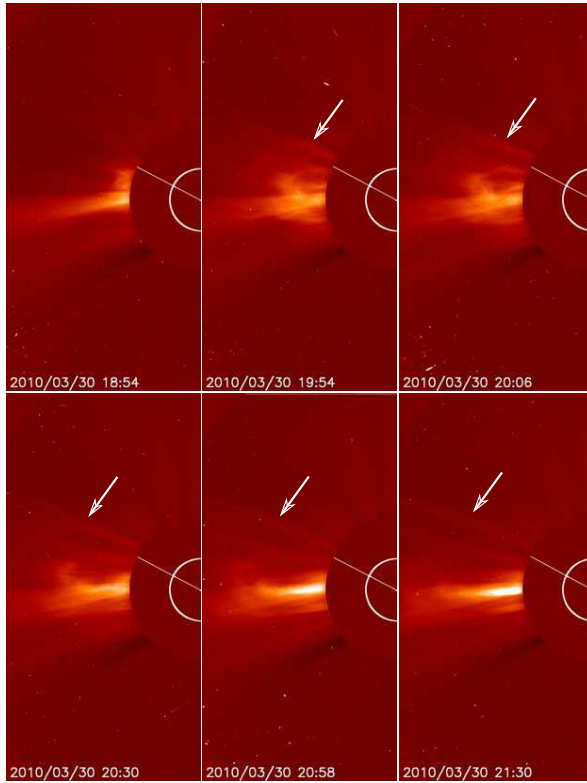


Fig. 3. SOHO/LASCO C2 registrations between 18:54 UT and 23:42 UT on 30 March 2010. The CME is first shown at 18:54 UT with a central position angle of 86° . The white radial line over-plotted on the occulting disk indicates the central PE position angle (55°). The white arrows point out the narrow CME loop above the PE, which is a part of the northern CME periphery.

ulations have also been carried out in order to understand stability of the confined eruptions (e.g. Török & Kliem, 2005; Guo et al., 2010; Démoulin & Aulanier, 2010; An & Magara, 2013).

2.2. Filament eruption on 2010 November 11

The event on 2010 November 11 presents the complex FE/flare/CME phenomenon. It occurred between 15:14 UT and 17:08 UT in AR NOAA 11123 (Fig. 4). The AR had a complex $\beta\gamma$ configuration that produced five GOES C-class flares, with the strongest one of class C4.7. For examination of this event was used a unique combination of ground- and space-based spectral and imaging observations to explore in detail both temporally and spatially the small-scale evolution of all three phenomena (Huang et al., 2014).

The filament activation was preceded of an increased activity in one of its footpoints. The dynamic activity prior to the FE was presented by sharp

brightness increase in the circular ribbon, together with simultaneous up- and down-flows of cool plasma taking place in the filament footpoint. A circular ribbon, together with simultaneous rising and falling material seen in the filament legs, strongly suggest a surge-like activity occurring at this place (see Huang et al., 2012). A surge-like event with a circular ribbon in one of the filament footpoints was determined to be the trigger of the filament destabilization. In addition, plasma draining in this footpoint was identified as the precursor for the filament eruption.

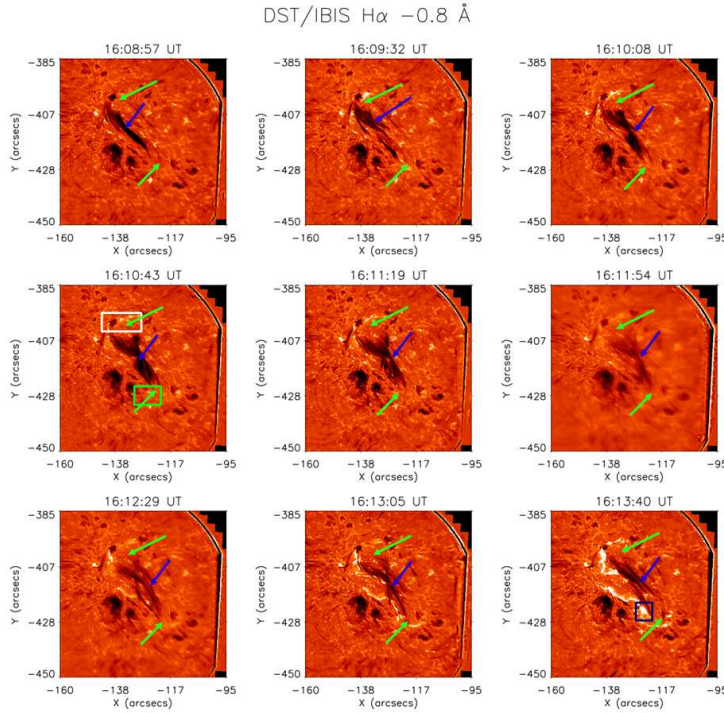


Fig. 4. The failed (or partial) filament eruption seen in $H\alpha -0.8 \text{ \AA}$. The blue arrows point at the rising twisted flux-ropes of the filament. The green arrows point at the foot-points of the filament. The white (North) and green (South) boxes outline the foot-points of the filament where the magnetic flux was derived from. The blue box is the flare kernel.

The FE showed two distinctive phases: the rising of the filament (15:59 – 16:09 UT), possibly triggered by the pre-flare activity, and its eruption (16:09 – 16:16 UT). The filament began to rise with a transverse component of the velocity of 8 km/s. During the slow rising phase, only part of it (approximately one quarter) underwent eruption. During the eruption phase, the velocity increased from 36 km/s to 85 km/s. As can be clearly seen, the part of the filament fell back. The filament rise and fall were

also seen in emission in all AIA channels. The erupting filament, seen in emission in these channels, suggests heating to temperatures as high as $\log T(\text{K}) = 5.8$. A 2π twist of the filament FR is clearly visible during its rising (best seen in $H\alpha - 0.8 \text{ \AA}$, at 16:11 UT). One cannot conclude with certainty whether this filament eruption can be classified as partial or failed. In spite of that, there was a clear indication that the FE pushed into the overlying loops which then erupted as part of the CME.

The FE evolution was accompanied by a GOES C4.3 flare. The flare evolution in $H\alpha$ observations before its decay phase revealed three phases, each with different energetics. The events that relate to each of these phases were determined by combining temporally and spatially the chromospheric, EUV, soft X-ray, and hard X-ray observations. Moreover, the formation of three flare ribbons, which occurred consecutively during these phases, were found. The timing of the ribbons formed during the second and third flare phases indicated that these events coincided clearly with the eruption phase of the filament that started at $\sim 16:09$ UT. This analysis clearly indicated that the flare was triggered by the filament destabilization and eruption.

The FE/flare event produced a relatively narrow CME (width 59° – 66°), comprising two clouds released with a time interval of ~ 10 min. The CME was first registered in SECCHI COR1 at 16:15 UT (Fig. 5). It propagated with an average speed of 367 km/s (minimum 250 km/s and maximum 595 km/s) as measured in SECCHI COR2 FOV. Two clouds were seen forming the CME, with the first one appearing at approximately 16:15 UT, followed by the second one displaced more to the south between 16:25 UT and 16:30 UT. The two parts of the CME reflect the complexity of energy release during the flare because they coincide with the two strong impulsive peaks recorded during the flare evolution.

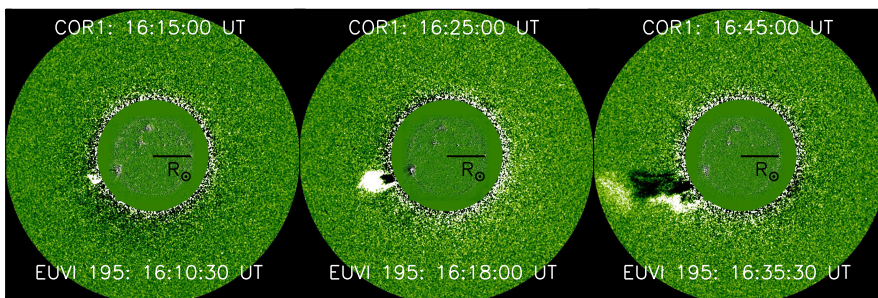


Fig. 5. Combination of STEREO A SECCHI/COR1 and EUVI 195 \AA images of the CME caused by the filament/flare sequence of events. Image reproduced from Huang et al. (2014).

2.3. Homologous prominence eruptions on 2006 August 22

The event on 2006 August 22 presents a sequence of four homologous non-radial PEs, which were observed at the southwestern solar limb between 04:48 UT and 18:30 UT (Fig. 6). The source of the four eruptions was a fragment of a filament located nearby the leading sunspot in AR 10904. The AR had $\beta\gamma/\beta\gamma$ configuration that rapidly changed to α/β -configuration on 2006 August 22. Morphologically, each of the PEs represents magnetic FR consisting of helically twisted thin magnetic threads filled with prominence plasma (Fig. 6) which presented surge-like behavior during the eruptions (Duchlev et al., 2014, 2016).

The homologous PEs were preceded by distinctive pre-eruptive prominence activation that was observed by Nobeyama Radioheliograph (NoRH) at a frequency of 17 GHz between 23:00 UT and 06:40 UT. The pre-eruptive phase represented a sequence of three activation episodes. Each episode contained pre-eruptive precursors such as a brightening and enlarging of the prominence body, followed by a small surge-like ejection from its southern end (Duchlev et al., 2016). The first three PEs were observed between 04:48 UT and 07:32 UT with the $H\alpha$ coronagraph at the National Astronomical Observatory Rozhen (NAO-Rozhen) (Duchlev et al., 2014). The fourth PE, that occurred 11 h after the third eruption, was observed in $H\alpha$ by the Polarimeter for Inner Coronal Studies (PICS) instrument at the Mauna Loa Solar Observatory (MLSO), Hawaii, between 17:08 UT and 18:30 UT (Fig. 6).

The first, second and fourth eruptions appeared as straight FRs showing surge-like behavior. They had similar kinematics exhibiting two main stages: a raising stage followed by a post-eruptive downflow stage, i.e. their height-time profiles were typical for confined PEs (Fig. 7). The first FR began to raise with a growing acceleration from 27.6 m/s^2 to 104.4 m/s^2 and velocity from 28 km/s to 111 km/s at a height of 50 Mm . Then, it rose with a constant velocity of 116 km/s up to a maximum height of 150 Mm . The second FR rose with an average linear velocity of 70 km/s up to a maximum height of 160 Mm (Duchlev et al. 2014). The fourth FR eruption was registered in a late stage (see, Duchlev et al., 2016) when the FR rose to the maximum height of 196 Mm with decreasing velocity from 160 km/s to 6 km/s and a negative acceleration of -72 m/s^2 .

During the post-eruptive stages, the prominence plasma flowed back to the chromosphere along the same trajectory. After the 1st eruption, the plasma drained back with a deceleration of -35.9 m/s^2 and the velocity decreased from 118.2 km/s to 56.1 km/s . After the 2nd FR eruption, the plasma flowed back with a linear velocity of 75 km/s (Duchlev et al., 2014). The downflow kinematics of the 4th eruption was more specific because the plasma initially flowed back to a height of 149 Mm with deceleration from -48 m/s^2 to 3.3 m/s^2 and velocity from 62 km/s to 15 km/s . Then, the acceleration changed from negative to positive and the velocity increased up to 26 km/s . The FR morphology evolution (e.g. its untwisting) was crucial factor for such kinematics (Duchlev et al. 2016).

The 3rd eruption, linked to a narrow CME, had a very different behavior. This eruption had a similar coronagraphic appearance and the same

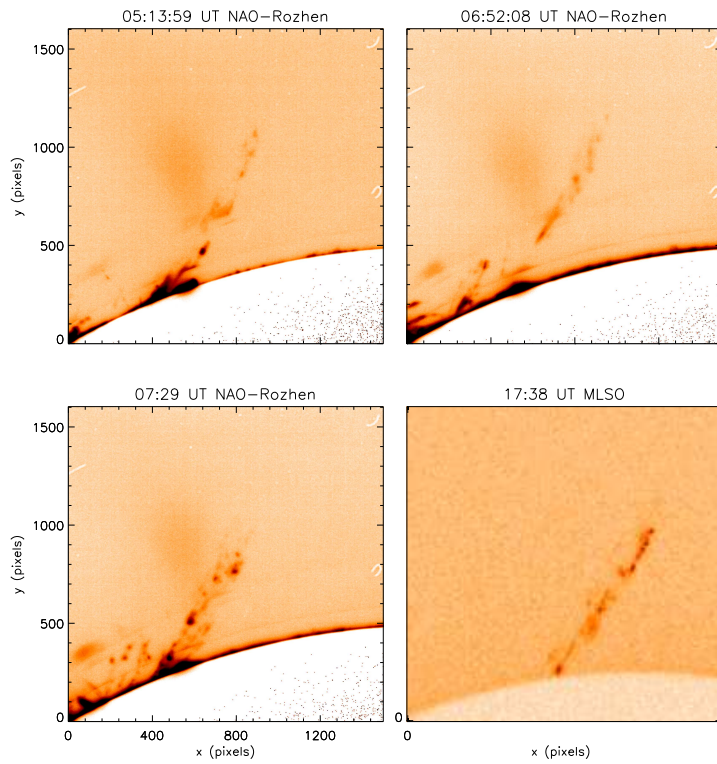


Fig. 6. The four prominence eruptions shown at their maximum heights by the $H\alpha$ observations of NAO - Rozhen and MLSO.

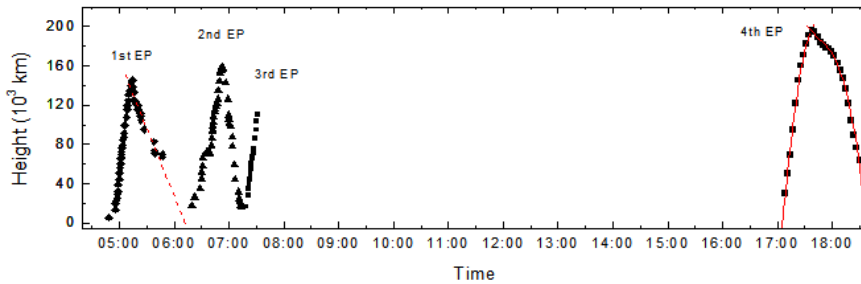


Fig. 7. Height-time profiles of the four homologous prominence eruptions on 22 August 2006.

non-radial propagation as the other three eruptions. It lasted only 13 minutes during which the FR rose with a constant velocity of 26 km/s up to a

height of 110 Mm. Afterward, the prominence FR began to fade gradually in the $H\alpha$ line to full disappearance, i.e. it showed signatures of thermal sudden disappearance (Ofman et al., 1998) that was followed by prominence/filament reformation (see, Duchlev et al., 2016).

The four PEs showed all signatures of homologous eruptive FRs (Li & Zhang 2013). Besides, they showed an additional signature of FR homology. They preserved the same non-radial propagations upwards in the corona, at almost the same deflection angle of $\sim 50^\circ$. Moreover, each consecutive PE in the homologous sequence, except the third one, reached greater height. This, according to DeVore & Antiochos (2008) and Cheng et al. (2013), suggests gradual weakening of the overlying magnetic field after each of the eruptions.

The LASCO C2 coronagraph observed four CMEs associated with the AR 10904 events on 2006 August 22 (Fig. 8). The first three weak and narrow CMEs in Fig. 8b were linked to the three pre-eruptive episodes observed by NoRH. Moreover, each of these events was associated with a weak B-class flare and an interplanetary type III burst in the WIND/WAVES dynamic spectrum. The third PE was linked to the fourth CME, B-class flare, a coronal metric type III radio burst at 164 MHz registered by the Nançay Radioheliograph (NRH) and WIND/WAVES type III burst.

The CME associated with the 3rd PE traveled along a coronal streamer. It first appeared at 09:12 UT and its onset, estimated by the linear approximation, is at 06:55 UT. The linear CME speed was 234 km/s and the second-order speed and acceleration at the CME final height were 163 km/s and -24.3 m/s^2 , respectively. The weak short-lived CME with angular width of 14° was observed only in the LASCO C2 FOV.

3. Eruptions of two nearby FRs of the same prominence

3.1. Eruptions of two coupled prominence FRs on 2014 May 4

The eruptive event was observed as a PE above the western limb in SDO/AIA FOV between 15:36 UT and 21:36 UT (Fig. 9, left), and at the southwest limb in EUVI B FOV from 15:36 UT to 21:30 UT (Fig. 9, right). In the EUVI A FOV the event was observed as a FE in a quiet solar region near the southwest solar limb between 16:14 UT and 21:00 UT (Fig. 9, middle), where the pre-eruptive state of the source region and filament initiation were observed. The erupted filament part was composed of two closely coupled FRs with the same, left-handed twist: top-located compact one (FR1) and bottom-located more diffuse one (FR2).

During the last stage of the prominence slow rising, the upper parts of the coupled FR1 and FR2 underwent interaction that led to their merging and, subsequently, to splitting. The magnetic threads in the upper part of FRs gradually brightened up. The brightening, well observed in all EUV lines, resulted in upward U-shaped structure forming along the interface of FRs' interaction. After brightening peak, the U-shaped structure began to fade accompanied by the FRs' splitting. When it disappeared the two FRs were already clearly separated. The EUV brightening could be interpreted as a signature of slow magnetic reconnection (Su et al., 2015). Such

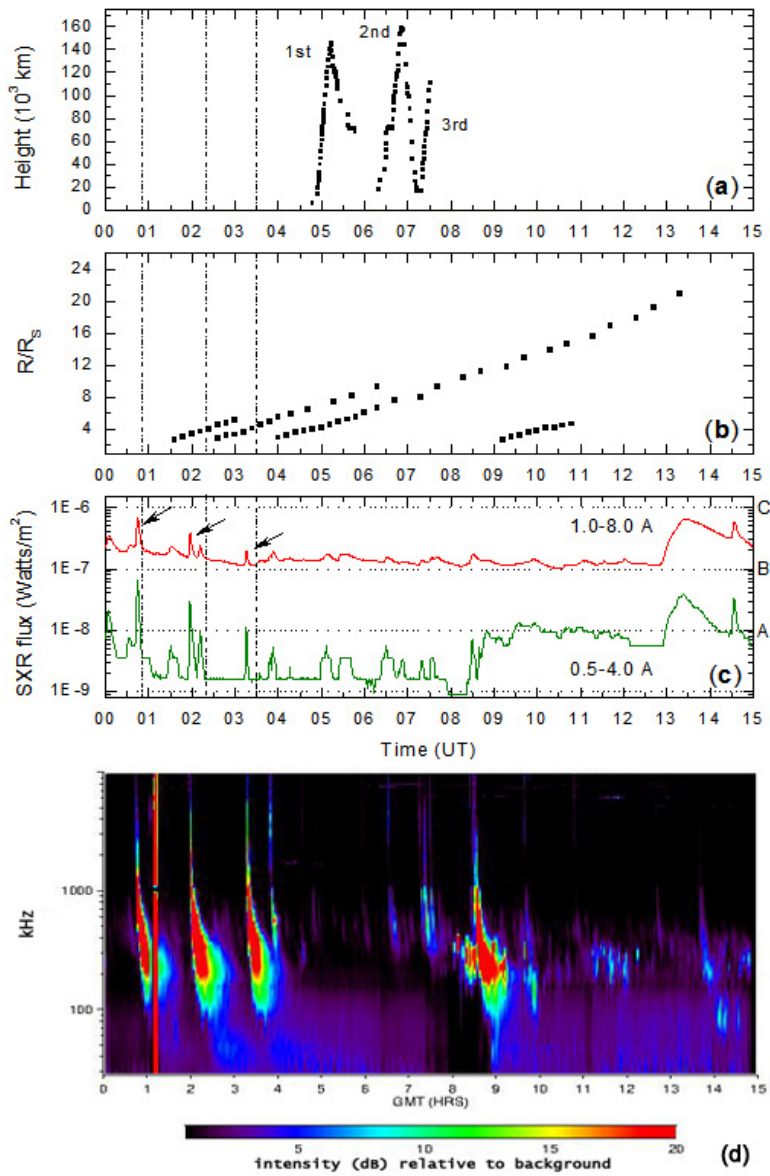


Fig. 8. (a) Height-time plots of the first three PEs. (b) Height-time plots of the CMEs, associated with AR 10904. (c) GOES-12 1-min soft X-ray fluxes. (d) WIND/WAVES RAD-1 and RAD-2 dynamic spectrum. The vertical dash-dotted lines in the panels a, b and c mark the times of maximum phase of the three pre-eruptive episodes. The black arrows in panel b point at the B-class flares linked to the pre-eruptive episodes. Panels b, c and d reproduced from Duchlev et al. (2016).

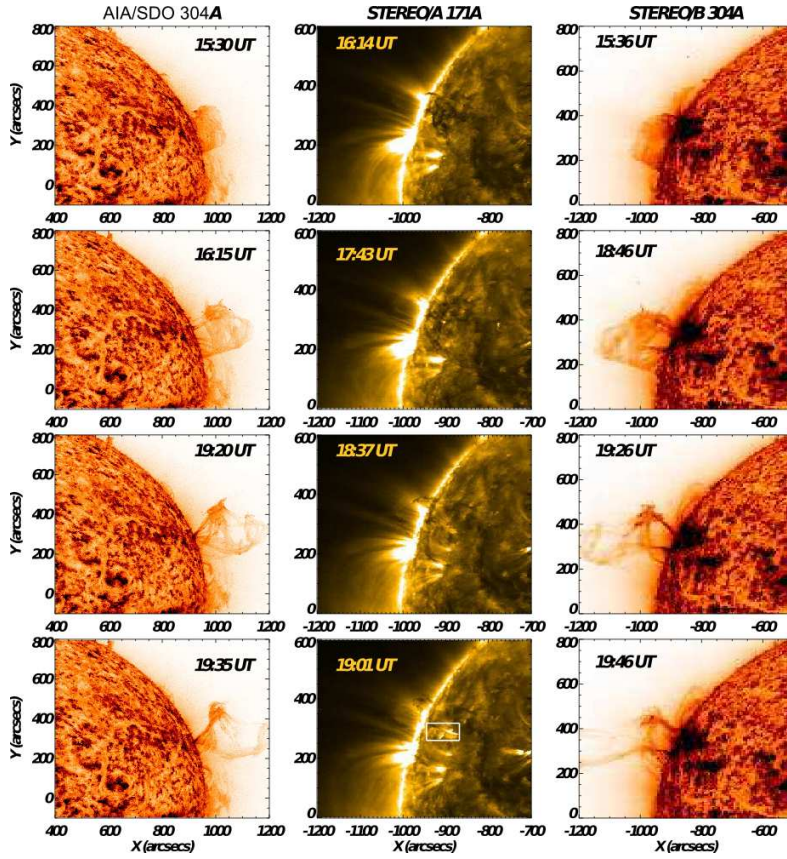


Fig. 9. Different stages of the PE evolution in three different instruments FOV: (left) AIA 304 Å reversed color images, (middle) STEREO A 171 Å images, (right) STEREO B 304 Å reversed color images. Image reproduced from Dechev et al. (2018a).

brightening evolution suggested mass and flux transfer which, according to Liu et al. (2012), must involve a transfer of current from the lower FR2 to the upper FR1. Moreover, accumulation of flux under the apex of FR1 can contribute to its twist, i.e. it affords the destabilization process (see, e.g. Kliem et al., 2014).

In the later stages of the eruption (19:30 UT), when the entire FR1 was still visible in the AIA FOV, its morphology distinctly exhibited a lot of left-handed twisted flux threads. At that time FR1 clearly showed left-handed kink writhe, i.e. counterclockwise rotation of its apex. After 19:30 UT FR2 showed a descending motion, accompanied by plasma draining and structure simplification. Later, some of the FR2 threads became recognizable, and at 20:00 UT FR2 exhibited maximum writhing of about $3/4$ turn (1.5π). At 20:55 UT the FR2 almost reached the initial height and its shape

became approximately the same as the original one, but with a strongly simplified structure. Therefore, the final stage of FR2 was its reformation at its original place. Hence, the big amount of FR2 kinking (Gilbert et al., 2007; Torok et al., 2010) and its reformation strongly suggested a failed type of eruption.

In the AIA 304 Å FOV, the FR1 slowly rose with velocities from 5.7 km/s to 31.3 km/s and accelerations between 0.2 m/s² and 4.9 m/s². It underwent a kink-induced partial eruption, which was associated with a slow CME. As a bright core in the CME cavity, the FR1 could be traced up to 15 R_{\odot} (Fig. 10). The kinked FR2 exhibited non-radial failed eruption and its kinematics showed two phases. The FR2 kinked loop underwent a short-time eruption in negligible height range of 10 Mm. Afterward it showed a long-lasting downward motion with velocities of several tens km/s to its original place.

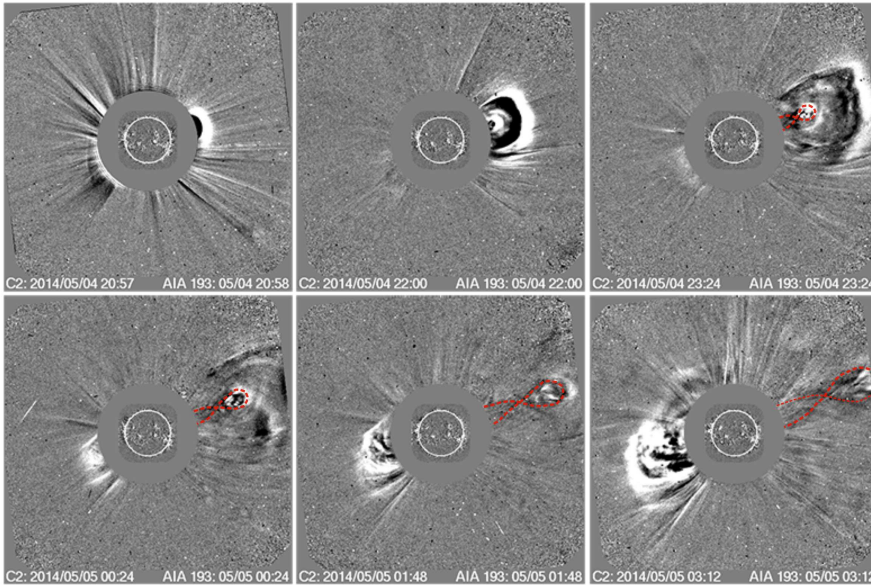


Fig. 10. Different stages of the CME evolution observed by LASCO/C2 coronagraph. The red dotted lines trace out the evolution of FR1 kinked structure. Image reproduced from Dechev et al. (2018a).

In the EUVI B 304 Å FOV, the FR1 showed two phases of eruption. The FR1 slow rising took place in the height range from 85 Mm to 133 Mm, where its velocity increased from 1.7 km/s to 14 km/s at accelerations between 0.13 m/s² and 3 m/s². During the fast phase FR1 rose with velocities from 14 km/s to 50 km/s and accelerations between 3.1 m/s² and 6.2 m/s². The FR2 evolution showed two phases - eruptive and post-

eruptive. Initially, FR2 slowly rose in a narrow height range (100-110 Mm) with velocities from 170 km/s to 75 km/s and an acceleration of -15.2 m/s^2 . Later, it entered in the post-eruptive phase, when FR2 gradually descended from 80 Mm to 54 Mm with velocities from 75 km/s to 21 km/s and an acceleration of -2.1 m/s^2 .

A CME associated with the FR1 eruption was well observed by the coronagraphs of SOHO/LASCO C2 and C3. The CME had an angular width of 106° and it exhibited classical three-part structure, with a bright leading edge, dark cavity, and a bright core (Fig. 10). In the late PE stage, the FR1 appeared as a bright CME core. Moreover, the evolution of FR1 kinked loop was clearly displayed in the LASCO C2 FOV. The close temporal and spatial relationship between the CME and FR1 are presented in (Fig. 10). The CME propagated with linear velocity of 329 km/s, or 2nd-order velocity of 342 km/s at constant acceleration of 0.8 m/s^2 . The apparent CME propagation could be traced up to a distance of $\sim 21 R_\odot$ in LASCO C3 FOV. Besides, in the LASCO C3 FOV, the core front gradually faded and at a distance of $18 R_\odot$ it fully disappeared, which suggests the FR1 underwent a successful eruption.

3.2. Interaction and eruption of two nearby prominence FRs on 2014 March 14

The source of the PE was a filament located along a PIL in a young short-lived AR SPoCa: SOL2014-03-14T04:081, still in its emergence phase. In pre-eruptive phase, the source region included several causally related activities (Dechev et al. 2018b). In a large scale, the filament was situated at the bottom of an ambient multiple-arcade helmet streamer. The event was observed as a PE in the SDO/AIA (Fig. 11, top) and STEREO-A/EUVI FOVs, while in the EUVI B FOV it was observed as a FE (Fig. 11, bottom).

The PE initially appeared at 07:33 UT on the east limb as a slow rising massive flux rope (MFR) and lasted until 11:48 UT. At 08:27 UT the tightly twisted bright flux rope (BFR) initiated by surge eruption (Dechev et al., 2018b) began slowly to rise beneath the MFR. This process lasted up to the PE fast-rise onset, when the BFR was already visible as a bright loop, merged with the MFR inner edge, forming in this way a single PE FR. Afterwards, the single FR underwent gradual brightening from the top downwards. Such brightening suggests subsequent reconnections that redistribute the magnetic flux between two FRs into a single FR. There are two possible processes of merging. First one depends on the properties of the flux rope configuration and perturbation and is susceptible to merging if the lower FR shows the stronger instability (Kliem et al., 2014). Another process, based on the Taylor relaxation model (Hussain et al., 2017), is reliable if the FRs have different twist degrees. In our case, the BFR has sufficiently bigger twist than the MFR.

During the early fast eruption phase, the bright single FR underwent EUV dimming in different parts of its body: at the top, in the middle part of the northern leg, and at its footpoints. The strongly heated plasma in these regions was well visible in all EUV lines. In addition, during the EUV dimming process a flare started at the PE vicinity that suggested a sympathetic casual relation between the PE and flare.

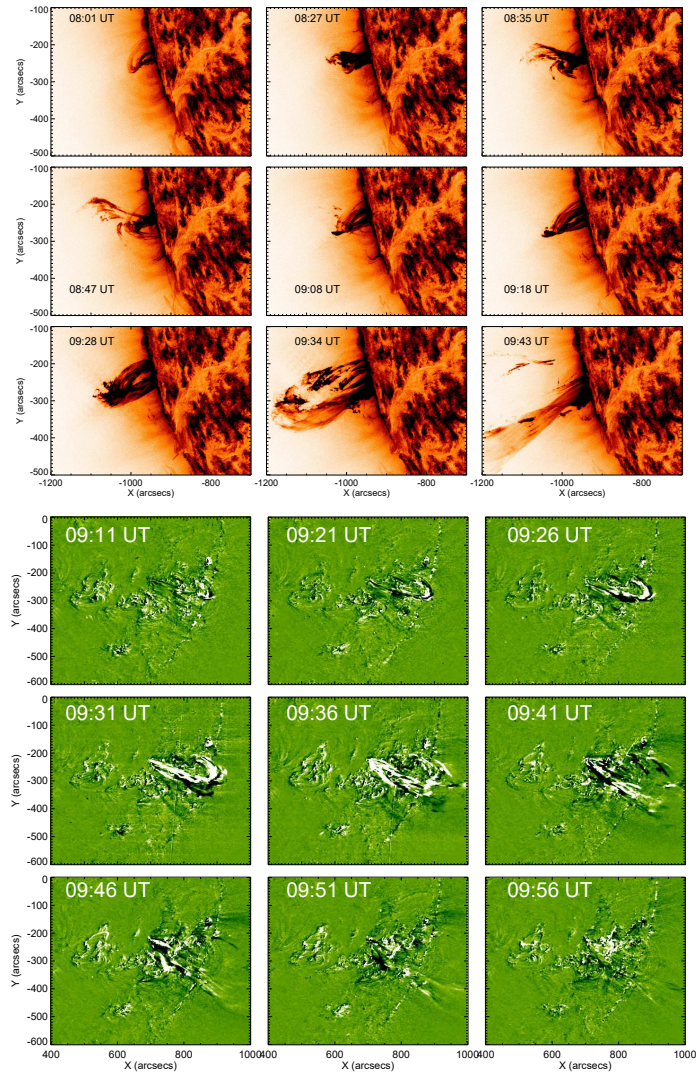


Fig. 11. (top) The evolution of the PE on 2014 March 14 in reversed color SDO/AIA 304 Å images. (bottom) The evolution of a FE on 2014 March 14 in STEREO B/EUVI 195 Å running difference images. Images reproduced from Dechev et al. (2018b).

Just after the onset of the PE strong acceleration, the single FR upper part began to split laterally, which is similar to the cases of partial eruptions (Liu et al., 2007). The splitting of MFR and BFR within the single FR could be explained by the transfer of magnetic flux from the lower to the upper rope (Kliem et al., 2014). Moreover, in some extent our case is in conformity with the scenarios of Kliem et al. (2014) for full eruption of

the double-FR, in which the dominant instability of the lower FR, acts as upward perturbation, applied to the upper FR.

The PE showed two distinctive phases: a slow rise phase and a fast acceleration phase. During the slow rise phase (08:00 - 09:02 UT), the PE rose in AIA FOV with an average speed of ~ 3 km/s, while in the EUVI A FOV (08:38 - 09:04 UT) it rose with speeds from 2 km/s to 12 km/s and accelerations from 1 m/s^2 to 11 m/s^2 . After 09:02 UT, the PE exponentially accelerated in the AIA FOV with speeds from ~ 3.5 km/s to ~ 280 km/s, while in the EUVI FOV its speeds increased from 12 km/s to 470 km/s at accelerations in the range 23-890 m/s^2 . It should be noted that in the EUVI A FOV, only the last 62 minutes of the slow raising phase were observed, because the PE position was of $\sim 25^\circ$ behind the EUVI A western limb. However, in the EUVI A FOV the eruptive phase was observed to higher altitudes, because its FOV ($1.7 R_\odot$) is bigger than the AIA FOV ($1.3 R_\odot$).

The appearing of a PE and an associated partial-halo CME below a multi-arcade helmet streamer was crucial for the BFR and MFR propagation and the CME morphology that was very different from the classical CME 3-part structure (Fig. 12). After the splitting of prominence compound FR during its eruption, the cool MFR propagated in a direction close to that of the southern unipolar streamer, while the thin hot BFR propagated below the bipolar streamer. The CME leading frontal loop was relatively faint, followed by the secondary apparent bright loop and the inhomogeneous cavity below them. The CME bright core presented a bi-component structure produced by the upper parts of cool MFR and hot BFR, which had quite different asymmetrical positions in the cavity (Fig. 12). Such bright core with hot and cool components was reported for the first time by Li and Zhang (2013) for a filament eruption. The partial-halo CME with width of 192° propagated with linear velocity of 469 km/s and 2nd-order velocity of 481 km/s at constant acceleration of 1 m/s^2 . The apparent CME propagation could be traced up to a distance of $\sim 21 R_\odot$ in LASCO C3 FOV. In the STEREO B COR2 FOV the CME core (MFR top) can be traced up to $15 R_\odot$.

4. Summary and discussion

Coronal mass ejections are generally associated with low coronal signatures, such as filament/prominence eruptions, jets, flares, or EUV waves (Alzate & Morgan, 2017). Moreover, the FE/PE is considered as one of the fundamental solar precursors of CMEs (Gopalswamy, 2003; Gopalswamy et al., 2006; Alzate & Morgan, 2017). This review is focused on five events of linked PEs and CMEs. Details for them are given in Table 1.

Events 1 and 2 present eruptions of single loop-like FRs with legs line-tied in the photosphere, observed on-limb (PE) and on-disk (FE), respectively. Event 1 represents kink-induced PE appearing in a quiet region plage and in strongly asymmetric position about the overlying CME. The type of eruption is rather failed because after the eruption, the source filament was partially rebuilt. Moreover, the global background magnetic fields might affect the dynamic behavior and type of filament eruptions and associated CMEs (e.g. Démoulin, 2008; Yang et al., 2012b, 2015 and references

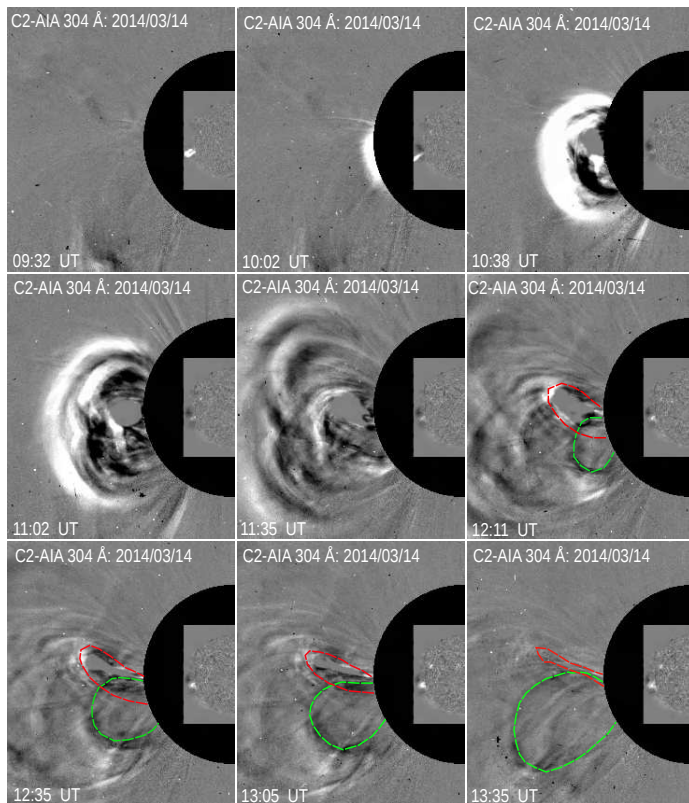


Fig. 12. A sequence of LASCO C2 and SDO/AIA 304 Å running difference images showing the progression of the 2014 March 14 prominence eruption as a bright core of partial-halo CME. The dashed lines in the last four frames trace the loops of EP FRs: green - MFR and red - BFR. Image reproduced from Dechev et al. (2018b).

therein). For example, whether the eventual type of a kink-induced eruptions, would be a full, a partial, or a failed eruption, strongly depends on the interaction between the erupting FR and magnetic environment and depends on the properties of the overlying magnetic field as well (e.g., Gilbert et al., 2007; Liu, 2008; Yang et al., 2012a, 2018, and references therein). The PE of event 1 has strongly asymmetric position below the CME complex arcade that can provide a relatively stronger confinement for flux rope eruptions than the symmetric background fields (see Liu et al., 2009; Shen et al., 2011).

Event 2 represents surge-triggered failed FE appearing in $\beta\gamma$ AR composed of eight sunspots, i.e. in a complex multi-flux system rich in GOES C-class flares. Magnetic flux emergence is believed to be the trigger for a surge formation (Jiang et al. 2007). The FE evolution leads to the appearance of C4.3 flare and relatively narrow CME. The CME exhibits specific morphology composed of two clouds and it could be assigned to so-called

unstructured (non 3-part) CMEs according to Hutton & Morgan (2015). The filament eruption can be classified as partial or failed. Unfortunately, the specific CME morphology did not help the distinct identification of the FE type.

Table 1. Table 1. Characteristics of the sampled events. (*) Speed and acceleration in SDO/AIA FOV. (**) Linear CME speed. (***) 2nd-order speed at a CME maximum distance.

Event	FR	Source region	PE type	Slow rise*	Fast rise*	CME
Event1 2010-03-30	1	quiet region	failed or partial	10 km/s	15-166 km/s 46-430 m/s ²	normal 724 km/s** 599 km/s***
Event2 2010-11-11	1	AR 11123 $\beta\gamma$	failed or partial	8 km/s	36-85 km/s	faint two parts 367 km/s** 595 km/s***
Event 3 2006-08-22	1st 2nd 3rd	AR 10904 $\alpha\beta$	failed failed failed	28-111 km/s 70 km/s	116 km/s 70 km/s 26 km/s	narrow 234 km/s** 163 km/s***
	4th		failed		160-6 km/s -72 m/s ²	
Event 4 2014-05-04	1st	quiet region	full or partial	1.7-14 km/s 0.13-3 m/s ²	14-50 km/s 3.1-6.2 m/s ²	normal 329 km/s** 342 km/s***
	2nd	quiet region	failed		170-75 km/s -15.2 m/s ²	
Event 5 2014-03-14	2	AR SOL2014- 03-14T04:08	full	\sim 3 kms	12-470 km/s 23-890 m/s ²	partial-halo 469 km/s** 481 km/s***

Event 3 presents one of the very rarely reported cases of quadruple homologous PEs. Four homologous eruptions of a single prominence FR occur in a $\beta\gamma/\beta\gamma$ AR on 2006 Aug 22. The erupting FRs exhibit surge-like propagation in the same strong non-radial direction ($\sim 50^\circ$ deflection). Four PEs are identified as failed (confined) and three of them (1st, 2nd and 4th) show kinematics that are typical for failed eruptions. The third PE is failed due to its thermal sudden disappearance in $H\alpha$ that occurs when the prominence is heated so, that it disappears in the cooler emission wavelengths, but appears in hotter EUV or X-ray lines (Ofman et al., 1998). This dramatic behavior is evidenced by a metric type III radio burst at 164 MHz and WIND/WAVES type III burst. The type III burst at 164 MHz slowly drifted outward that could be considered as radio signature of the

reorganization of the overlaying magnetic arcade, resulting in the magnetic field restructuring at the edges of the associated CME (e.g. Pick et al., 2005).

The homologous PEs appear beneath the northern flank of a bipolar coronal streamer and are offset from the streamer centers and the associated CME. The strong asymmetry of the overlying field plays a crucial role not only for confinement of erupting FRs, but also for their deflection from radial direction of propagation. A number of observations revealed that solar eruptions in the low corona such as jets, FEs, and CMEs, can be channeled and guided by ambient large-scale magnetic fields during their early stages (Nistico et al., 2015). Some typical events that can interact with erupting FRs and can cause (through interchange reconnection (Crooker et al., 2002; Yang et al., 2015)) their non-radial propagations are: ARs (Sterling et al., 2011; Sun et al., 2012; Kliem et al., 2013), coronal holes (Lugaz et al., 2011; Makela et al., 2013; Zheng et al., 2016), and helmet streamers (Bemporad et al., 2005; Moore & Sterling, 2007; Yang et al., 2011) or pseudostreamers (Bi et al., 2013; Lynch & Edmondson, 2013; Yang et al., 2015, 2018).

Event 4 presents a rarely reported case of slow kink-induced eruptions of two coupled FRs of the same prominence in a quiet region, which interacted during the eruption (Dechev et al., 2018a). Initially, the top FR1 and bottom FR2 coherently rise up and just before their eruption they interact showing merging, followed by long-lasting splitting. The interactions are accompanied by dynamic EUV brightening that is considered as a signature of slow reconnection, which suggests helicity flux transfer from the lower FR2 to the upper FR1. In a scenario of a similar FRs configuration, Kliem et al. (2014) find that the lower more unstable FR enables the eruption of the upper one, followed by downward motion and possible destruction of the lower FR. The considerable kink-writhe ($\pi/2$ and 1.5π) of FR1 and FR2, the apparent mass draining in the FRs legs and flare-ribbons beneath them, strongly suggest kink instability to be a driver of the eruptions. However, the interactions of FR1 and FR2 also played a crucial role for their eruption type and eruptive behavior. FR1 undergoes full eruption, which produces the bright core of a 3-part CME. Kink evolution of FR1 loop as a bright core may be well traced up to the edge of LASCO C2 FOV ($6R_{\odot}$), when its kink writhe reaches almost 1π . The FR2 undergoes a failed eruption and after reaching a maximum height, it descends and simplifies in structure. Finally it is rebuilt at its original place.

Event 5 presents an eruption of two interacting nearby prominence FRs, which also belongs to rarely reported cases (Dechev et al., 2018b). The PE source is a filament in young AR located below a multi-arcade streamer. Initially the PE slow rise as an MFR and, 54 min later, the second tightly twisted BFR, triggered by surge in the filament channel (Dechev et al., 2018b) began to rise beneath the MFR. In view of the FRs interaction, the PE evolution can be divided in four stages. The first stage represents the pre-eruptive activity in AR that leads to the surge appearing and BFR onset. In the second stage, BFR rise below the MFR and just before the eruptive phase it interacted and merged through reconnection with MFR, forming a single PE FR with a bright inner edge. The third stage cov-

ers the early eruptive phase when the prominence rapidly rises as single FR. Meantime, the single FR undergoes gradual brightening from the top downwards, followed by EUV dimming in different parts of its loop. Such EUV brightening suggests continuous merging between two FRs within the compound one that via reconnections lead to redistribution of the magnetic flux from the lower BFR to the upper MFR. Most probably, this process triggers the flare appearance during this stage. The fourth stage starts just after the onset of strong acceleration, when the single PE FR begins to split laterally at its upper part, which is similar to the cases of partial eruptions (e.g. Liu et al., 2007). After the FR and MFR splitting, they rise with growing speeds in quite different non-radial directions and realize full eruption, which later produces a bi-component bright core of partial-halo CME. According to one of numerical scenarios of Kliem et al. (2014), such full eruption could be driven by the stronger torus instability of the lower flux rope that is very similar to the eruption of a single torus-unstable flux rope.

Acknowledgements

The data for these studies are used courtesy of the SDO/AIA and HMI, STEREO/SECCHI, SOHO/LASCO, IBIS/NSO Sacramento Peak, PICS/MLSO, NoRH, NRH, GOES and WIND/WAVES science teams. The research, presented here was co-funded by the Bulgarian National Science Fund under Grants DH 08-1/13.12.2016 and DN 18-13/12.12.2017.

References

- An, J. M., & Magara, T. 2013, *ApJ*, **773**, 21
 Aulanier G., Török, T., Démoulin P., DeLuca E. E., 2010, *ApJ*, **708**, 314
 Aulanier, G., 2014, in IAU Symp., **300**, 184
 Aulanier, G., DeVore, C. R., Antiochos, S. K., 2006, *ApJ*, **646**, 1349
 Bao, X., Zhang, H., Lin, J., Stenborg, G. A., 2007, *A&A*, **463**, 321
 Bemporad, A., Sterling, A. C., Moore, R. L., & Poletto, G., 2005, *ApJL*, **635**, L189
 Bi, Y., Jiang, Y. C., Yang, J. Y., et al., 2013, *ApJ*, **773**, 162
 Bi, Y., Jiang, Y., Li, H., Hong, J., Zheng, R., 2012, *ApJ*, **758**, 42
 Brueckner, G.E., Howard, R.A., Koomen, M.J., et al., 1995, *Solar Phys.*, **162**, 357
 Chae J., Wang H., Qiu J., Goode P. R., Strous L., Yun H. S., 2001, *ApJ*, **560**, 476
 Chatterjee, P., & Fan, Y., 2013, *ApJL*, **778**, L8
 Chen, B., Bastian, T. S., & Gary, D. E., 2014a, *ApJ*, **794**, 149
 Chen, P. F., & Shibata, K., 2000, *ApJ*, **545**, 524
 Cheng, B., Kliem, B. and Ding, M. D., 2018, *ApJ*, **856**, 48.
 Cheng, X., Zhang, J., Ding, M.D., et al., 2013, *ApJ*, **769**, L25
 Chertok, I. M., Grechnev, V. V., Hudson, H. S., & Nitta, N. V., 2004, *JGR*, **109**, 1
 Crooker, N. U., Gosling, J. T., & Kahler, S. W., 2002, *JGRA*, **107**, 1028
 Dechev, M., Koleva, K., Duchlev, P., 2018a, *New Astronomy*, **59**, 45
 Dechev, M., Duchlev, P., Koleva, K., 2018b, *BlgAJ*, **28**, 60
 Démoulin, P., 2008, *Ann. Geophys.*, **26**, 3113
 Démoulin, P., & Aulanier, G., 2010, *ApJ*, **718**, 1388
 Dere, K. P., Brueckner, G. E., Howard, R. A., Koomen, M. J., et al., 1997, *Solar Phys.*, **175**, 601
 DeVore, C. R., & Antiochos, S. K., 2008, *ApJ*, **680**, 740
 DeVore, C. R., Antiochos, S. K., Aulanier, G., 2005, *ApJ*, **629**, 1122
 Duchlev, P., Koleva, K., Madjarska, M. S., Dechev, M., 2016, *New Astronomy*, **48**, 66.
 Duchlev, P., Koleva, K., Dechev, M., Petrov, N., 2014, *BlgAJ*, **21**, 92

- Engvold, O., 1998, in IAU Colloq. 167: New Perspectives on Solar Prominences, ed. D. F. Webb, B. Schmieder, & D. M. Rust, ASP CS, Vol. 150, 23
- Feynman, J., & Martin, S. F., 1995, *JGR*, **100**, 3355
- Forbes, T. G., 2000, *JGR*, **105**, 23153
- Forland, B. C., Gibson, S. E., Dove, et al., 2013, *Solar Phys.*, **288**, 603
- Fuller, J. & Gibson, S. E., 2009, *ApJ*, **700**, 1205
- Fuller, J., Gibson, S. E., de Toma, G., & Fan, Y., 2008, *ApJ*, **678**, 515.
- Gibson, S. E., & Fan, Y., 2006, *ApJL*, **637**, L65
- Gibson, S. E., Foster, D., Burkepile, J., de Toma, G., & A., S. 2006, *ApJ*, **641**, 590
- Gilbert, H. R., Alexander, D., & Liu, R. 2007, *Solar Phys.*, **245**, 287
- Gilbert, H. R., Holzer, T. E., Burkepile, J. T., & Hundhausen, A. J., 2000, *ApJ*, **537**, 503
- Gopalswamy, N. 2015, in Solar Prominences, ed. J.-C. Viall & O. Engvold, ASSL Vol. 415, Switzerland: Springer International Publishing, 381
- Gopalswamy, N., Shimojo, M., Lu, W., et al., 2003, *ApJ*, **586**, 562
- Green, Lucie M., Török Tibor, Vršnak, Bojan, et al., 2018, *Space Sci. Rev.*, **214**, 46.
- Guo, Y., Ding, M. D., Schmieder, B., et al., 2010, *ApJL*, **725**, L38
- Habbal, S. R., Druckmüller, M., Morgan, H., et al., 2010, *ApJ*, **719**, 1362
- Hood, A. W., & Priest, E. R., 1981, *Geophys. Astrophys. Fluid Dyn.*, **17**, 297
- Howard, R. A., Moses, J. D., Vourlidas, A., et al., 2008, *Space Sci. Rev.*, **136**, 67
- Hutton, J. & Morgan, H., 2015, *ApJ*, **812**, 35
- Illing, R. M., & Hundhausen, A. J., 1986, *JGR*, **91**, 10951
- Ji, H., Wang, H., Schmahl, E. J., et al., 2003, *ApJL*, **595**, L135
- Jiang, Y. C., Chen, H. D., Li, K. J., et al., 2007, *A&A*, **469**, 331
- Jiang, Y., Yang, J., Hong, J., et al., 2011, *ApJ*, **738**, 179
- Jiang, Y., Yang, J., Zheng, R., et al., 2009b, *ApJ*, **693**, 1851
- Jiang, Y., Yang, J., Wang, H., et al., 2014, *ApJ*, **793**, 14
- Jiang, Y.-C., Bi, Y., Yang, J.-Y., et al., 2009a, *RAA*, **9**, 603
- Joshi, A. D. and Srivastava, N., 2011, *ApJ*, **730**, 104.
- Joshi, N. C., Schmieder, B., Magara, T., et al., 2016, *ApJ*, **820**, 126
- Joshi, N. C., Srivastava, A. K., Filippov, B., et al., 2013, *ApJ*, **771**, 65
- Joshi, N. C., Srivastava, A. K., Filippov, B., et al., 2014, *ApJ*, **787**, 11
- Kienreich, I. W., Veronig, A. M., Muhr, N., et al., 2011, *ApJL*, **727**, L43
- Kim J.-H., Yun H. S., Lee S., et al., 2001, *ApJ*, **547**, 85
- Kliem, B., Su, Y. N., van Ballegooijen, A. A., & DeLuca, E. E., 2013, *ApJ*, **779**, 129
- Kliem, B., Török, T., Titov, V. S., et al., 2014, *ApJ*, **792**, 107.
- Kong, D. F., Yan, X. L., Xue, Z. K., 2013, *Ap&SS*, **348**, 303
- Kumar, P., Srivastava, A. K., Filippov, B., et al., 2011, *Solar Phys.*, **272**, 301
- Kumar, P., Manoharan, P. K., Uddin, W., 2010, *ApJ*, **710**, 1195
- Kuridze, D., Mathioudakis, M., Kowalski, A. F., et al., 2013, *A&A*, **552**, A55
- Labrosse, N., Heinzel, P., Vial, J.-C., et al. 2010, *Space Sci. Rev.*, **151**, 243.
- Lemen, J.R., Title, A.M., Akin, D.J., et al., 2012, *Solar Phys.*, **275**, 17.
- Leroy, J.-L., 1989, in Dynamics and Structure of Quiescent Solar Prominences, E. R. Priest (ed.), 77.
- Li, T., & Zhang, J., 2013, *ApJ*, **778**, 29
- Li, Y. & Ding, M.-D., 2012, *RAA*, **12**, 287
- Lin, J., Soon, W., & Baliunas, S. L., 2003, *New Astron. Rev.*, **47**, 53
- Linton, M. G., Dahlburg, R. B., Antiochos, S. K., 2001, *ApJ*, **553**, 905
- Liu, C., Lee, J., Karlický, M., et al., 2009a, *ApJ*, **703**, 757
- Liu, K., Wang, Y., Shen, C., & Wang, S., 2012, *ApJ*, **744**, 168.
- Liu, L., Wang, Y., Liu, R., et al., 2017, *ApJ*, **844**, 141
- Liu, R., Alexander, D., Gilbert, H. R., 2007, *ApJ*, **661**, 1260
- Liu, R., Gilbert, H. R., Alexander, D., & Su, Y., 2008, *ApJ*, **680**, 1508
- Liu, R., Kliem, B., Török, T., et al., 2012, *ApJ*, **756**, 59.
- Liu, Y., Su, J., Xu, Z., et al., 2009b, *ApJL*, **696**, L70
- Lugaz, N., Downs, D., Shibata, K., et al., 2011, *ApJ*, **738**, 127
- Lynch, B. J., & Edmondson, J. K., 2013, *ApJ*, **764**, 87
- Mackay, D. H., Karpen, J. T., Ballester, J. L., et al., 2010, *Space Sci. Rev.*, **151**, 333.
- Mäkelä, P., Gopalswamy, N., Xie, H., et al., 2013, *Solar Phys.*, **284**, 59
- Maričić, D., Vršnak, B., & Rosa, D., 2009, *Solar Phys.*, **260**, 177.
- Martin, S. F., 1998, *Solar Phys.*, **182**, 107.
- McCauley, P. L., Su, Y. N., Schanche, N., et al., 2015, *Solar Phys.*, **290**, 1703
- Moore, R. L., & Sterling, A. C., 2007, *ApJ*, **661**, 543

- Nistico, G., Zimbardo, G., Patsourakos, S., et al., 2015, *A&A*, **583**, A127
- Ofman, L., Kucera, T. A., Mouradian, Z., & Poland, A. I., 1998, *Solar Phys.*, **183**, 97
- Panasenco, O., Martin, S. F., Velli, M., & Vourlidas, A., 2013, *Solar Phys.*, **287**, 391
- Parenti, S., 2014, *Living Reviews in Solar Physics*, **11**, 1.
- Pick M, Malherbe J-M, Kerdraon A, Maia D.J.F., 2005, *ApJ*, **631**, L97
- Reeves, K. K., Gibson, S. E., Kucera, T. A., & Hudson, H. S., 2012, *ApJ*, **746**, 146.
- Schmieder, B., Démoulin, P., Aulanier, G., 2013, *Advances in Space Research*, **51**, 1967
- Schmit, D. J. & Gibson, S. E., 2011, *ApJ*, **733**, 1
- Schrijver, C. J., & Title, A. M., 2011, *JGRA*, **116**, 4108
- Schrijver, C. J., Aulanier, G., Title, A. M., et al., 2011, *ApJ*, **738**, 167
- Schrijver, C. J., Elmore, C., Kliem, B., Török, T., & Title, A. M., 2008, *ApJ*, **674**, 586.
- Shen, Y., Liu, Y., & Su, J., 2012, *ApJ*, **750**, 12
- Shen, Y.-D., Liu, Y., & Liu, R., 2011, *RAA*, **11**, 594
- Sterling, A. C., Moore, R., & Harra, L. K. 2011, *ApJ*, **743**, 63
- Sterling, A. C., Moore, R. L., Berger, T. E., Bobra, M., et al., 2007, *PASJ*, **59**, 823
- Su, J., Liu, Y., Kurokawa, H., et al., 2007, *Solar Phys.*, **242**, 53
- Su, Y., Surges, V., van Ballegoijen, A., et al., 2011, *ApJ*, **734**, 53
- Sun, X., Hoeksema, J. T., Liu, Y., et al., 2012, *ApJ*, **757**, 149
- Thompson, W. T., 2011, *JASTP*, **73**, 1138
- Titov, V. S., Mikic, Z., Török, T., et al., 2012, *ApJ*, **759**, 70
- Török, T., & Kliem, B., 2005, *ApJL*, **630**, L97
- Török T., & Kliem, B., 2007, *Astron. Nachr.*, **328**, 743
- Török, T., Berger, M. A., & Kliem, B., 2010, *A&A*, **516**, 49
- Török, T., Panasenco, O., Titov, V. S., et al., 2011, *ApJL*, **739**, L63
- Tripathi, D., Gibson, S. E., Qiu, J., et al., 2009, *A&A*, **498**, 295
- Vasquez, A. M., Frazin, R. A., & Kamalabadi, F., 2009, *Solar Phys.*, **256**, 73
- Wang, D., Liu, R., Wang, Y., et al., 2018, *ApJ*, **869**, 177
- Williams, D. R., Török, T., Démoulin, P., et al., 2005, *ApJ*, **628**, L163
- Yan, X.-L., Qu, Z.-Q., Kong, D.-F., 2012, *ApJ*, **754**, 16
- Yang, Bo; Jiang, Yunchun; Yang, Jiayan, et al., 2016, *ApJ*, **830**, 16.
- Yang, J., Dai, J., Chen, H., et al., 2018, *ApJ*, **862**, 86
- Yang, J., Jiang, Y., Bi, Y., et al., 2012a, *ApJ*, **749**, 12
- Yang, J., Jiang, Y., Xu, Z., Bi, Y., & Hong, J., 2015, *ApJ*, **803**, 68
- Yang, J., Jiang, Y., Zheng, R., et al., 2011, *Solar Phys.*, **270**, 551
- Yang, J., Jiang, Y., Zheng, R., et al., 2012b, *ApJ*, **745**, 9
- Yang, Liheng, Yan, Xiaoli, Li, Ting, et al., 2017, *ApJ*, **838**, 131
- Zhang, J., & Wang, J., 2002, *ApJ*, **566**, L117
- Zhang, Q. M. and Ji, H. S., 2018, *ApJ*, **860**, 113
- Zheng, R., Chen, Y., Du, G., & Li, C., 2016, *ApJL*, **819**, L18
- Zhou, G. P., Wang, J. X., Zhang, J., et al., 2006, *ApJ*, **651**, 1238
- Zhu, C., Liu, R., Alexander, D., Sun, X., McAteer, R. T. J., 2015, *ApJ*, **813**, 60
- Zhukov, A. N., & Veselovsky, I. S., 2007, *ApJ*, **664**, L131